Draft version April 18, 2025
Typeset using LaTeX **preprint2** style in AASTeX631

Constraining Nuclear Molecular Gas Content with High-resolution CO Imaging of GOALS Galaxies

James Agostino,[1] Anne M. Medling,[1] Loreto Barcos-Muñoz,[2,3] Vivian U,[4]
Mynor Rodríguez Vásquez,[5] George C. Privon,[6,7,8] Claudia Cicone,[9] Lee Armus,[10]
Jorge Moreno,[11,12] Claudio Ricci,[13,14] Yiqing Song,[15,16] Christopher C. Hayward,[17]
Katherine Alatalo,[18,19] and David B. Sanders[20]

[1]*Ritter Astrophysical Research Center and Department of Physics & Astronomy, University of Toledo, Toledo, OH 43606, USA*
[2]*National Radio Astronomy Observatory, 520 Edgemont Road, Charlottesville, VA, 22903, USA*
[3]*Department of Astronomy, University of Virginia, 530 McCormick Road, Charlottesville, VA, 22903, USA*
[4]*4129 Frederick Reines Hall, Department of Physics and Astronomy, University of California, Irvine, CA 92697, USA*
[5]*Instituto de Investigación en Ciencias Físicas y Matemáticas USAC, Ciudad Universitaria, Zona 12, 01012, Guatemala, Guatemala*
[6]*National Radio Astronomy Observatory, 520 Edgemont Road, Charlottesville, VA 22903*
[7]*Department of Astronomy, University of Florida, P.O. Box 112055, Gainesville, FL 32611, USA*
[8]*Department of Astronomy, University of Virginia, 530 McCormick Road, Charlottesville, VA 22904, USA*
[9]*Institute of Theoretical Astrophysics, University of Oslo, PO Box 1029, Blindern, 0315 Oslo, Norway*
[10]*IPAC, California Institute of Technology, 1200 East California Boulevard, Pasadena, CA 91125, USA*
[11]*Department of Physics and Astronomy, Pomona College, Claremont, CA 91711, USA*
[12]*The Observatories of the Carnegie Institution for Science, 813 Santa Barbara Street, Pasadena, CA 91101, USA*
[13]*Instituto de Estudios Astrofísicos, Facultad de Ingeniería y Ciencias, Universidad Diego Portales, Avenida Ejercito Libertador 441, Santiago, Chile*
[14]*Kavli Institute for Astronomy and Astrophysics, Peking University, Beijing 100871, China*
[15]*European Southern Observatory, Alonso de Córdova, 3107, Vitacura, Santiago, 763-0355, Chile*
[16]*Joint ALMA Observatory, Alonso de Córdova, 3107, Vitacura, Santiago, 763-0355, Chile*
[17]*Center for Computational Astrophysics, Flatiron Institute, 162 Fifth Avenue, New York, NY 10010, USA*
[18]*Space Telescope Science Institute, 3700 San Martin Drive, Baltimore, MD 21211, USA*
[19]*William H. Miller III Department of Physics and Astronomy, Johns Hopkins University, Baltimore, MD 21218, USA*
[20]*Institute for Astronomy, University of Hawaii, 2680 Woodlawn Drive, Honolulu, HI 96822*

ABSTRACT

We present measurements of the cool molecular gas mass around the nuclei of two gas-rich mergers, **III Zw 035 and IRAS F01364−1042**, whose **enclosed masses (M_{enc}) within the central 40-80 pc would be overmassive if attributed entirely to the supermassive black hole mass (SMBH) and** compared to SMBH-galaxy scaling relations. Our gas mass measurements are derived from Atacama Large Millimeter/submillimeter Array (ALMA) Band 6 long-baseline observations of CO(J=2-1) and 230 GHz continuum emission at 14-20 pc resolution, which probes below the resolving limit of the previous black hole mass measurements. Subtracting molecular gas mass from these enclosed masses is not enough to **reconcile with BH-galaxy relationships**, but independently measuring enclosed mass using the cold CO(2-1) gas does shift the black holes down to their expected values. Still, these ALMA data **reveal molecular gas masses of ∼4×10^{7} to ∼7×10^{8} M$_{\odot}$ within 70 pc of these black holes which could challenge some black hole accretion models that assume nuclear gas like this has no angular momentum**.

1. INTRODUCTION

Every massive galaxy in our universe is thought to host a supermassive black hole (SMBH) in its center. These SMBHs typically **contain** masses millions or billions times the mass of our Sun. Their gravitational **sphere** of influence is tiny (of order ∼1-100 pc, **the radius of which can be defined as r$_{\rm SOI}$ = GM$_{\rm BH}/\sigma_*^2$; see Yoon 2017**) when compared to the typical kpc to hundreds of kpc scale sizes of galaxies. Despite this, a number of galaxy-wide properties correlate with the mass of the central SMBH. These are the so-called black hole mass scaling relations, where SMBH mass scales with host galaxy properties like bulge luminosity (Kormendy 1993; Ho 1999; Marconi & Hunt 2003; McConnell & Ma 2013), stellar mass (Silk & Rees 1998; Magorrian et al. 1998; Kormendy & Gebhardt 2001; McLure & Dunlop 2002; Häring & Rix 2004; Bennert et al. 2011; Cisternas et al. 2011), and bulge velocity dispersion (Gebhardt et al. 2000; Merritt & Ferrarese 2001; Tremaine et al. 2002; Gültekin et al. 2009; Beifiori et al. 2012; McConnell & Ma 2013). The mechanism driving these relations is not well understood and the search for a physically-motivated picture for the co-evolution is an active area of research (see Kormendy & Ho 2013 and Heckman & Best 2014 for reviews and Bennert et al. 2021 for a recent study on local galaxies).

One of the major uncertainties in placing galaxies on the SMBH-galaxy scaling relations is a precise measurement of the mass of the black hole. Even with very-long-baseline interferometry, the region near the event horizon can only be directly "observed" around the nearest, most massive SMBHs (Event Horizon Telescope Collaboration et al. 2019). **Depending on the target and data available, multiple approaches can be taken to measure SMBH mass. Some of these methods include reverberation mapping (Clavel et al. 1991; Horne et al. 2004; Vestergaard & Peterson 2006a; Cackett et al. 2021), Schwarzschild modeling (Schwarzschild 1979; Faber & Jackson 1976; Lauer et al. 1995; Kormendy et al. 1997; Cretton et al. 1999; Gebhardt et al. 2000; van den Bosch et al. 2008; Walsh et al. 2012), direct measurements of stellar orbits (Ghez et al. 2008; Genzel et al. 2010), dynamical modeling of stars and gas in circumnuclear disks (>1 pc) (Cappellari 2008; Barth et al. 2009; Medling et al. 2011; U et al. 2013;Medling et al. 2014), and empirically-calibrated proxies (e.g. Vestergaard & Peterson 2006b; Morgan et al. 2010; Bentz et al. 2013; U et al. 2022).**

In this paper, we refer to a parent sample of nine SMBH **M$_{\rm enclosed}$** ≤ 77 **mas** masses within gas rich mergers derived via gas and stellar kinematics in Medling et al. (2015). These **enclosed mass** measurements use data from Keck/OSIRIS adaptive optics (AO) and target galaxies from the Great Observatory All-sky LIRG Survey (GOALS, Armus et al. 2009). In the K-band, these data use the CO (2-0) and (3-1) bandheads to trace kinematics of young stars along with **emission from** Brγ and H$_2$ $^{\rm 3D}$Barolo (Di Teodoro & Fraternali 2015) **transitions** for **the** kinematics of the gas. LIRGs (luminous infrared galaxies) emit an excess of light in the infrared (L$_{IR}$ > 10^{11} L$_{\odot}$ by definition; Sanders & Mirabel 1996) powered by vigorous activity from **either star formation or AGN, or both**. Based on dynamical (enclosed mass) measurements from Medling et al. (2015), the masses of these nine SMBHs lie above canonical black hole mass scaling relations: supermassive black hole mass (M_{BH}) vs. stellar velocity dispersion ($\sigma_\star$), total stellar mass ($M_\star$), and bulge luminosity ($L_{H,bulge}$). Non-LIRG spiral galaxies do not typically lie above scaling relations (Davis et al. 2018; Davis et al. 2019), and whether most LIRGs do remains in question. Overmassive black holes present a challenge to the canonical understanding of gas-rich mergers, which predicts that these black holes will grow more in an upcoming quasar phase — placing them in even greater conflict with scaling relations (Mirabel & Sanders 1988; Hopkins et al. 2008b; Hopkins et al. 2008a).

The results from Medling et al. (2015) were surprising but came with a caveat: the resolution of the Keck/OSIRIS+AO data does not probe all the way down to the **SMBH event horizon**. Those dynamically-derived SMBH mass measurements in Medling et al. (2015) are a mass enclosed within the **FWHM of the** data, 77 mas, meaning they could include **extended mass**. This paper is focused on quantifying exactly how much molecular gas mass exists within that limit, then completing an independent enclosed mass measurement for comparison. Medling et al. (2019) performed a pilot study focused on measureing molecular gas mass in one of these galaxies that host double nuclei, NGC 6240. Using Atacama Millimeter/submillimeter Array (ALMA) Band 6 CO(J=2-1) and continuum data to measure molecular gas mass, they found that in the northern nucleus, the black hole shifts down to scaling relations after the gas mass correction, as up to 89% of the previously measured enclosed mass could be attributed to gas rather than the black hole. In contrast, the **dynamical mass of the** southern nucleus **consists of up to only** 11% gas mass, leaving it above scaling relations. The following work estimates the amount of molecular gas mass in two other gas-rich, merging LIRGs with the purpose of understanding whether or not these galaxies host overmassive black holes. **Such confirmation would be further evidence for an accretion paradigm in which the SMBH grows before the global galaxy properties in scaling relations, which is contrary to the timeline of accretion in typical systems (Hopkins 2012; Cen 2012; Anglés-Alcázar et al. 2017**.

In this Paper we determine whether the amount of gas present within the resolving limit of the original dynamical mass measurements accounts for the observed disagreement with scaling relations. We then measure an independent enclosed mass using the CO(2-1) kinematics. This paper is structured as follows. Section 2 details the CO(2-1) measurements obtained from the ALMA and how the imaging process of these measurements was conducted. Section 4 explains how we calculated molecular gas mass estimates via both CO(2-1) and ALMA Band 6 continuum. Section 5 describes independent enclosed mass measurements using the same CO(2-1) cubes and how they compare to the Medling et al. (2015) enclosed masses. Section 6 contextualizes these results within the picture of scaling relations and what those results mean for our current picture of the co-evolution of merging gas-rich galaxies and their SMBHs.

The two galaxy merger systems featured in this paper are III Zw 035 and IRAS F01364−1042. III Zw 035 is at $z = 0.02744$ and **R.A.** = 01h44m30.50 s, **dec.** = +17d06m05.0 s with a total infrared luminosity $\log(L_{\rm IR}/L_\odot) = 11.64$. IRAS F01364−1042 is at z = 0.04823 and **R.A.** = 01h38m52.921 s, **dec.** = -10d27m11.42 s with a total infrared luminosity $\log(L_{IR}/L_\odot) = 11.85$ (Armus et al.

2009). Infrared luminosities of these galaxies and others in the GOALS survey can be found in Armus et al. (2009). **If III Zw 035 or IRAS F01364−1042 host AGNs, they must be dust-obscured.**

In this work, we use cosmological parameters of $H_0 = 70$ km s^{-1} Mpc^{-1}, $\Omega_m = 0.28$, and $\Omega_\Lambda = 0.72$ (Hinshaw et al. 2009). To calculate spatial scales and luminosity distances for III Zw 035 and IRAS F01364−1042 we use Ned Wright's Cosmology Calculator (Wright 2006). III Zw 035 has a scale of 554 pc arcsec^{-1} and IRAS F01364−1042 has a scale of 1012 pc arcsec^{-1}.

2. MEASUREMENTS AND IMAGING

The nuclei of III Zw 035 and IRAS F01364−1042 were observed with Keck-OSIRIS+AO in 2010 and 2011 (Medling et al. 2014). This integral field spectroscopy was used to measure dynamical masses at a resolution of 77 mas (Medling et al. 2015). As our science goal is to resolve the inner-most molecular gas in these galactic nuclei, our Band 6 observations were taken in ALMA's second-most extended configuration, C43-9 (PI Medling, project codes 2018.1.01123.S and 2019.1.00811.S). III Zw 035 was observed on 2019 June 20th for 4178 s (maximum recoverable scale [MRS] = 0.4") and IRAS F01364−1042 was observed on 2021 August 30th for 1689 s (MRS = 0.5") as well as in the C43-8 configuration on 2021 August 8th for 2541 s (MRS = 0.8"). For all measurement sets we follow the standard calibration pipeline and manually examined each measurement set to make sure flagging was complete. Then, for IRAS F01364−1042 we concatenated both measurement sets, checking for any inconsistencies in the relative weightings (rms) of each configuration. Compared to only using the configuration 9 measurement set the combined measurement sets give an rms that is a factor of $\sim\sqrt{2}$ lower and improves our signal by approximately the same value because of the increased effective exposure time and uv-sampling of the slightly more compact C43-8 configuration. Next, we imaged the line-free channels to produce continuum maps for each galaxy. This included avoiding not only the CO(2-1) line in both galaxies, but also lines like CS(5-4) and HC_3N which are prominent in the core of III Zw 035. We then perform continuum subtraction in the uv-plane and image the spectral window containing CO, producing a spectral cube for each galaxy. After imaging **with Briggs weighting (Briggs 1995;** `robust` $= -0.5$), our achieved **synthesized beam** resolutions (FWHMs) for **the data sets used in our analysis for** IRAS F01364−1042 and III Zw 035 respectively, are 41 and 30 mas for the spectral cubes and 29 and 26 mas for the continuum images. All of these data are firmly under the resolution used in the prior dynamical measurements. For III Zw 035, we achieved a root mean square (rms) of 1.11 mJy beam^{-1} in a channel width, Δv, of 10.4 km s^{-1} and a continuum rms of 0.033 mJy beam^{-1} while for IRAS F01364−1042 we achieved a rms of 0.43 mJy beam^{-1} in a channel width, Δv, of 11.2 km s^{-1} and a continuum rms of 0.029 mJy beam^{-1} . Table 1 lists relevant properties of these measurement sets and Figure 1 shows Hubble I-Band images (**GO-10592; PI: Evans**) of both of III Zw 035 and IRAS F01364−1042 overlaid with ALMA Band 6 CO(2-1) contours. **These contours were made using CO(2-1) imaged at a slightly lower resolution** than the dataset we use for our analysis (`robust` = 0.5).

We use the Common Astronomy Software Applications (*CASA*, CASA Team et al. 2022) package developed by the NRAO, ESO, and NAOJ to do this imaging. **tclean**, a routine within *CASA*, takes the measured visibilities and reconstructs a sky model. One of the **tclean** parameters that is part of the Briggs weighting scheme (Briggs 1995), `robust`, adjusts how different parts of the uv-plane (in

Fourier space) are weighted. To test the impact of the `robust` parameter on our results, we performed our analysis on a range of values (-0.5, 0, 0.5, 2). For our galaxies using a `robust` parameter of -0.5 loses less than 10% of flux to diffuse CO emission compared to the default pipeline value of (0.5) and provides the benefit of producing an image with **a narrower** beam FWHM.

Achieving the highest available spatial resolution matches our science goal by probing gas mass as close to the black hole as possible and so we chose `robust` $= -0.5$ as our default imaging for the analysis in this paper (both for CO and continuum).

3. MORPHOLOGY

3.1. *III Zw 035*

As defined by the merger classification from Stierwalt et al. (2013) in optical wavelengths, III Zw 035 is a pre-merger. This means that this galaxy and its companion have not yet had their first encounter. Figure 2 shows ALMA Band 6 CO, and continuum, along with a moment 1 (velocity) map of CO(2-1) for III Zw 035 and IRAS F01364$-$1042. The high resolution $\sim$26 mas molecular gas emission in III Zw 035 reveals a resolved core in CO with a peak integrated intensity that is slightly offset (5-10 pc) from the center of Band 6's continuum emission ($\sim$ 230 GHz). Continuum contours highlight several resolved clumpy substructures about 20-30 pc away from the central CO source. Previously, Pihlström et al. (2001) found clumps of OH maser and 18 cm continuum emission in similar positions around the central source. Further inspection of the ALMA data cubes in these clumps shows the presence of CS(5-4), a good dense gas tracer (Wang et al. 2011). The clumpy nature of this dense gas tracer and evidence from previous observations could indicate that there are star-forming clumps around III Zw 035's core. These clumps may also be part of a forming or otherwise evolving torus or ring around III Zw 035's nucleus, as distances of the clumps to the core are typical (10s of pc) for these sorts of structures (e.g. García-Burillo et al. 2021). CO(2-1) is not apparent in all of these clumps. Additional matched resolution data at other wavelengths, such as deeper ALMA Band 7 and Band 3 continuum, are necessary to further constrain the nature of this distribution of mass.

The CO moment 1 maps (Figure 2, bottom left) show strong disk-like rotation across the major axis of the galaxy, similar to what is seen in H_2 and Brγ (Medling et al. 2014). III Zw 035 also **show** evidence of a molecular outflow along the minor axis seen in the H_2 and Brγ maps in U et al. (2019), as well as in CO(1-0) at lower resolution in Lutz et al. (2020). III Zw 035's outflow can also be seen in CO(2-1) and it will be discussed in detail in a future work.

3.2. *IRAS F01364-1042*

Toward the opposite end of the merger spectrum, IRAS F01364$-$1042 is classified as a late-stage merger in Stierwalt et al. (2013). The two galaxies have their nuclei in the same envelope at the center of the system. As seen in Figure 2, compared to III Zw 035, the brightest CO(2-1) emission in IRAS F01364$-$1042 has an edge-on disk-like morphology that traces the continuum emission well, with a central source that seems to be marginally resolved. Similar to III Zw 035, it shows disk-like rotation in the high-resolution CO(2-1) imaging, with symmetrical velocity gradients on either side of the disk that match well to the H_2 and Paα maps at $\sim$2-3$\times$ coarser resolution in Medling et al. (2014). The CO(2-1) data presented in this work show evidence of the presence of an outflow, along the minor axis, originating from the nucleus. This outflow is also supported by MIRI H_2 and ALMA CO(1-0) maps (Song et al in prep.)

4. COMPUTING NUCLEAR GAS MASS

Galaxy	D_L (Mpc)	Merger Stage	Resolution (pc)	Freq. (GHz)	CO Flux (Jy km s^{-1})	Cont. Flux (mJy)
III Zw 035	110	Pre-Merger	13.62	224.38	1.617	5.042
IRAS F01364−1042	209.9	Late-Stage	19.23	219.84	8.791	2.796

Table 1. List of galaxy and observational properties used in this work. All data were taken in the long baseline ALMA 12m configuration. The frequency column shows the observed CO(2-1) frequencies. The merger stage definitions are from Stierwalt et al. (2013) where pre-merger is defined as galaxies prior to their first encounter and late-stage describes two nuclei in a common envelope (but that still show signs of a merger). Fluxes listed are integrated flux within the 77 mas aperture used throughout this work. **Absolute flux uncertainties in ALMA Band 3 and Band 6 data are 5 and 10%, respectively (Cortes et al. 2023).**

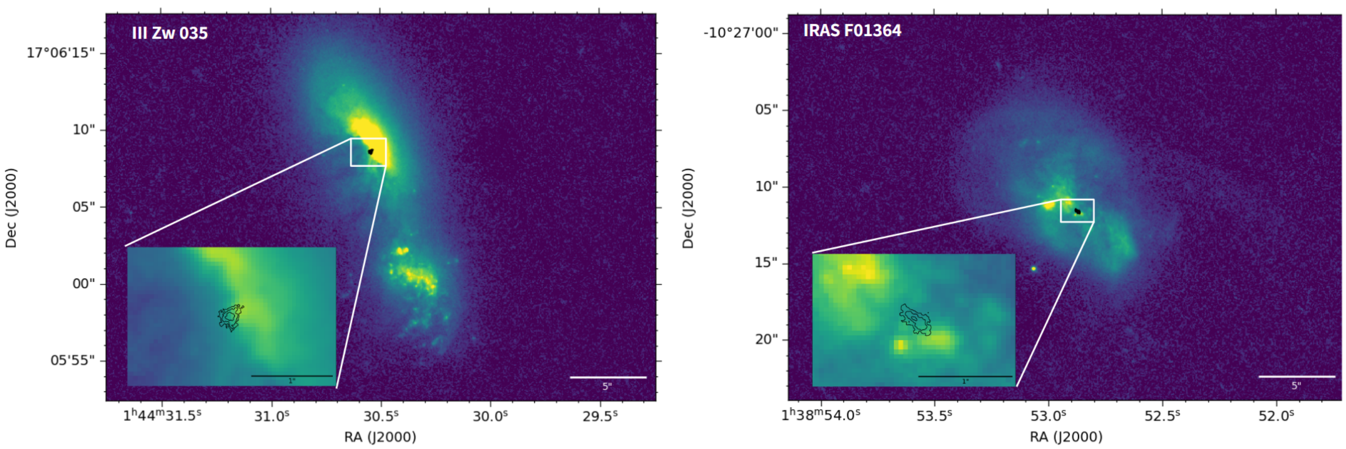

Figure 1. I-Band Hubble ACS images (**GO-10592; PI: Evans**) of III Zw 035 (left) and IRAS F01364−1042 (right) with CO(2-1) moment 0 contours overlaid in black. Moment 0 contours are from $10^{-0.4}$ to $10^{0.5}$ Jy beam^{-1} km s^{-1} for III Zw 035 and $10^{-0.8}$ to $10^{0.5}$ Jy beam^{-1} km s^{-1} for IRAS F01364−1042 in 7 logarithmically-spaced intervals. III Zw 035's companion galaxy still retains much of its large-scale structure, while in IRAS F01364−1042 the two are in a later stage of the merger process.

Our goal in this work is to calculate the amount of the nuclear molecular gas mass that falls within the resolution limit of Keck-OSIRIS+AO ($\sim$ 77 mas). Following Medling et al. (2019), in this section we describe our two main methods of calculating molecular gas mass. Additionally, we perform independent enclosed mass estimates, for comparison to Medling et al. (2015), through position-velocity (PV) diagrams in Section 5. We summarize and comment on the results of these analyses in Section 6.

As in Medling et al. (2019), we measure nuclear gas masses to compare with enclosed masses derived from stellar and gas kinematics from Medling et al. (2015). We include these original BH masses for III Zw 035 and IRAS F01364−1042 in the top row of Table 2. In this study we do not include comparisons to III Zw 035's enclosed warm gas mass because of high uncertainties attributed to the H_2 and Brγ outflow seen alone its minor axis U et al. (2019). For IRAS F01364−1042, we use the enclosed masses derived via gas kinematics, which could be impacted by the potential outflowing component; however, no stellar dynamics-based mass is available.

4.1. *Gas mass via CO(2-1)*

Although most interstellar gas is in the form of H_2 in LIRG nuclei, its net-zero dipole moment

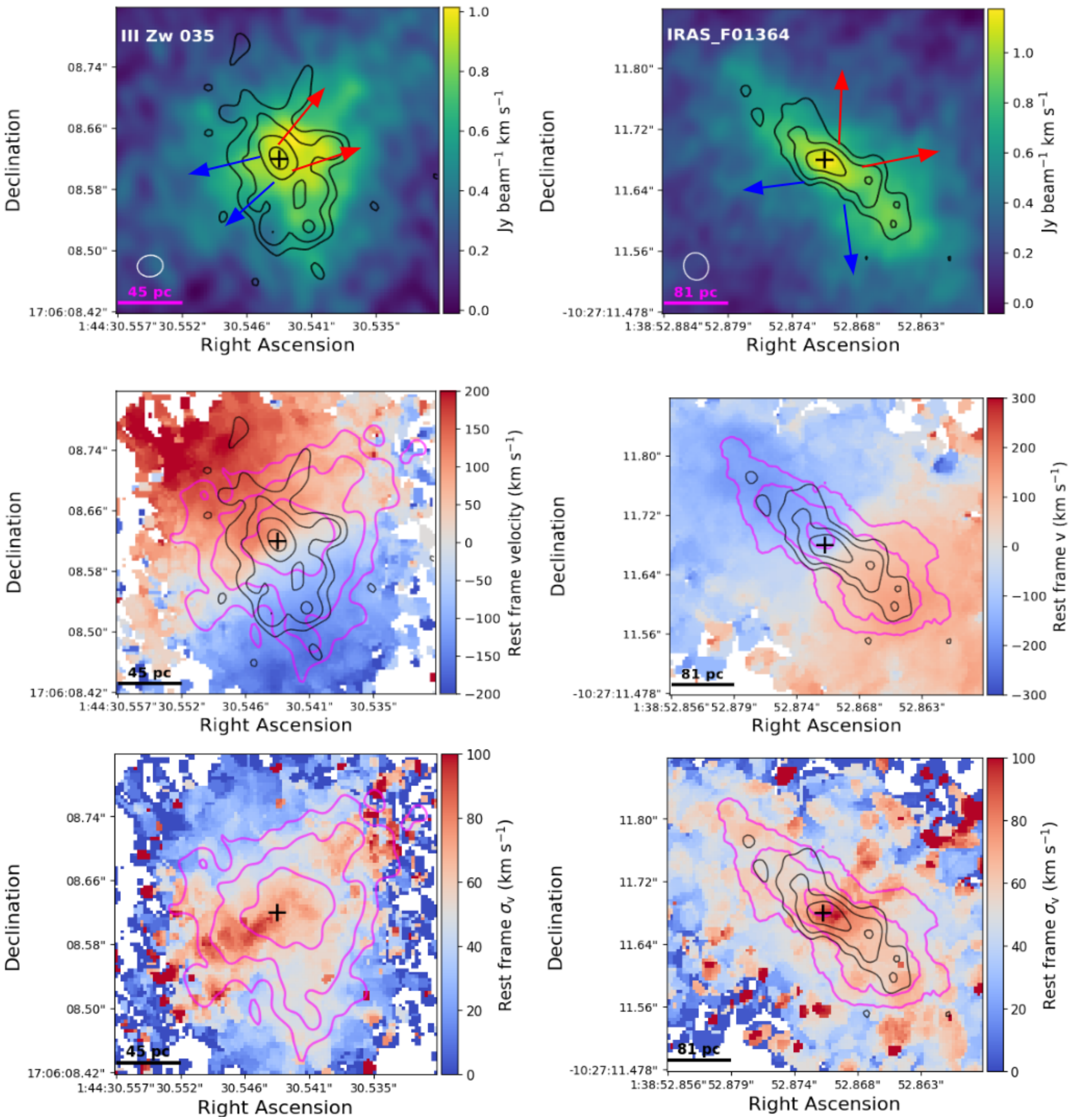

Figure 2. *Top:* CO(2-1) moment 0 (integrated intensity) maps for III Zw 035 (left) and IRAS F01364−1042 (right) with Band 6 continuum contours at 230 GHz for III Zw 035 and 228 GHz for IRAS F01364−1042 with levels at 3, 6, 12, 24, 48 × (rms) Jy beam^{-1} (rms values are 32.7 × and 29.4 × μJy beam^{-1} for III Zw 035 and IRAS F01364−1042 respectively). White ellipses indicate the beam sizes of the CO images (33 x 28 for III Zw 035 and 43 x 40 mas for IRAS F01364−1042. *Bottom; Middle:* CO(2-1) moments 1 (velocity) and 2 (velocity dispersion) maps. Black contours are the same as in the top two panels for continuum, while magenta contours are moment 0 contours from $10^{-0.4}$ to $10^{0.5}$ Jy beam^{-1} km s^{-1} for III Zw 035 and $10^{-0.8}$ to $10^{0.5}$ Jy beam^{-1} km s^{-1} for IRAS F01364−1042 in 7 logarithmically-spaced intervals. Velocity maps for both galaxies are clipped to a 3σ CO(2-1) detection. Continuum center, where we expect the black hole to be located, is indicated by a black cross. Red and blue arrows indicate the directionality and relative velocities of the molecular outflows.

makes it difficult to observe directly in luminous galaxies. Carbon monoxide is often used as a tracer molecule in its place (Solomon et al. 1972; Wilson et al. 1974; Scoville & Solomon 1975; Burton et al. 1975).

To calculate a molecular gas mass from our spectral cube we start with the full, 1.875 **(in GHz)** wide cube, then, in python, integrate across the channels with CO emission in each pixel. To determine if a channel has CO emission in it, we use a combination of visual inspection of the individual channel maps and integrated spectra in a rectangular region made in *CASA*. This produces a moment 0, or flux map of CO(2-1). Then, to calculate radial, integrated values we step outward in a box shape. Each radial step expands the box in two pixels in each x($\pm$1) and y($\pm$1) direction. The same radial stepping method is used in Section 4.2. To convert to mass we must first translate the CO line flux to CO line luminosity $L'_{CO(2-1)}$. For this we apply the equation from Solomon & Vanden Bout (2005):

$$L'_{CO(2-1)} = (3.25{\times}10^{7}) S_{CO} \Delta v (\nu_{obs}^{-2} D_L^2 (1+z)^{-3}) \quad \text{K kms}^{-1}\text{pc}^2 \tag{1}$$

where $f_\nu d\nu$ is the flux of the CO(2-1) emission (Jy km s^{-1}), ν_{obs} is the observed frequency (**in** GHz), and D_L is the luminosity distance (Mpc).

To convert from this line luminosity to mass we use the conversion factor α_{CO}. This conversion factor varies depending on where it is being applied, and the inclination angle of the galaxy. For example, on >600 pc scales, Sandstrom et al. (2013) find mean $\alpha_{CO_{(1-0)}}$ values ranging from 2.9 to 8.2. In NGC 3351, using $\sim$ 100 pc resolution ALMA data, Teng et al. (2022) find intensity-weighted values between 1.11 and 1.79 on 2 kpc scale, and find that the conversion factor is lower in inflow regions. Medling et al. (2019) used an $\alpha_{CO(2-1)}$ conversion factor calibrated spatially by Cicone et al. (2018) for the nuclear regions of NGC 6240. NGC 6240 is a local, merging LIRG like our systems, but it does host X-ray detected AGN and a clear double nucleus, unlike our systems.

In this work, we use the $\alpha_{CO(1-0)}$ **= 2.3 ± 1.2** from Cicone et al. (2018) and scale it to $\alpha_{CO(2-1)}$ by independently measuring r_{21} ($r_{21} = L'_{CO(2-1)}/L'_{CO(1-0)}$) at 100 mas resolution in both III Zw 035 and IRAS F01364−1042 (57 and 98 pc, respectively). **To measure this new r_{21} we created beam-matched images by first smoothing the CO(2-1) data to the CO(1-0) data (project code 2017.1.01235.S; PI: Barcos-Muñoz) by using *CASA*'s imsmooth task, which performs a Fourier-based convolution to the CO(1-0) beam in which we used a Gaussian kernel.** We then used the smoothed image to measure the line luminosities in the same 154 $\times$ 154 mas box used in our analysis. The new $\alpha_{CO(2-1)}$ value for III Zw 035 is calculated as:

$$\begin{aligned}\alpha_{CO(2-1)} &= \frac{\alpha_{CO(1-0)}}{r_{21}} = \frac{2.3 \pm 1.2}{0.762 \pm 0.1} \\ &= 3.017 \pm 1.23 \, M_\odot (\text{K km s}^{-1} \text{ pc}^2)^{-1}.\end{aligned} \tag{2}$$

and the same calculations are done for IRAS F01364−1042 which has a r_{21} = 0.772 ± 0.09 and $\alpha_{CO(2-1)}$ = 2.98 ± 1.25$M_\odot$(K km s^{-1} pc^2)$^{-1}$. **Uncertainties on r_{21} are attributed to the ALMA Band 3 and 6 flux uncertainties of 5 and 10% respectively (Diaz Trigo et al. 2019).** Using these $\alpha_{CO(2-1)}$ estimates rather than adopting the value from Cicone et al. (2018) increases the final gas (H_2 and helium) masses calculated in III Zw 035 and IRAS F01364−1042 by factors of 1.31 and 1.30, respectively.

The use of low-J CO lines as tracers of molecular gas has been explored for decades; α_{CO} or similar conversion factors have been calibrated for both the Milky Way and other galaxies (e.g. as reviewed by Dickman 1978, Combes 1991, and Bolatto et al. 2013). Montoya Arroyave

et al. (2023) measure a median $\alpha_{\rm CO(1-0)}$ = 1.7 ± 0.5 $M_\odot$ in 37 ULIRGs (ultra-luminous infrared galaxies, $L_{\rm IR} > 10^{12} L_\odot$) and 3 LIRGs (see also Herrero-Illana et al. 2019). Sandstrom et al. (2013) found that in the central kpc of 26 starburst galaxies, $\alpha_{\rm CO(1-0)}$ is a factor of ∼2 smaller than in the larger scale disk. Each of these studies found median $\alpha_{\rm CO(1-0)}$ values lower than the typical global value for the Milky Way (4.4 $M_\odot$(K km s^{-1} $pc^2)^{-1}$); Bolatto et al. 2013). These measurements were done on larger scales than the ones we make our enclosed mass measurements in, but suggest that globally-calibrated $\alpha_{\rm CO(1-0)}$ values cannot be trusted for analysis on nuclear scales. The $\alpha_{\rm CO(2-1)}$ we adopt here is therefore uncertain particularly compared to larger scale estimates of $\alpha_{\rm CO(1-0)}$, **because of the lack of studies which robustly calibrate these nuclear conversion factors on < 50 pc scales in LIRGs. In this work we attempt to mitigate for these uncertainties by using the highest resolution calibrated $\alpha_{\rm CO(1-0)}$ from Cicone et al. (2018) for NGC 6240, a merging (U)LIRG.**

The CO(2-1) flux profiles, which are multiplied by $\alpha_{\rm CO(2-1)}$ to obtain a mass profile, are shown in the top two rows of Figure 3. Inside the 77 mas Keck-OSIRIS resolution limit achieved in Medling et al. (2015) we find (4.23±2.12)× 10^7 $M_\odot$ of molecular gas mass for III Zw 035 and (6.68±3.49) × 10^8 $M_\odot$ of molecular gas mass for IRAS F01364−1042 within 43.7 and 76.9 pc, respectively. Fractionally these values account for between ∼1 and ∼52% (including 1σ errors) of the previously determined enclosed masses (see Table 2 for details).

4.2. *Gas mass via dust continuum*

Another way of estimating the central molecular gas mass is by measuring the cospatial dust mass using our mm-wavelength continuum imaging. For LIRGs, the mm/sub-mm continuum flux densities are typically dominated by thermal dust emission (U et al. 2012). Continuum measurements start with the same aperture as in Section 4.1 (a 154 x 154 mas square), integrating flux density as the box grows outward. We then use the calibrated dust continuum flux density ratio to H_2 from Scoville et al. (2016). This calibration improves on the Scoville et al. (2015) relation used for Arp 220, but it assumes a globally-derived, mass weighted dust temperature of 25 K. **In the sample of ULIRGs from U et al. (2012), the average global T_D was found to be moderate at ∼25-45 K.** Other recent studies have shown that luminosity-weighted nuclear dust temperatures can be much higher than this (e.g. Sakamoto et al. 2021), and so we explore a range of temperatures from 100-500 K for our primary analysis.

As our continuum-based measurements use a relation that assumes the emission is from dust, for them to be accurate we have to ensure that any contaminants to that emission are removed. Some of the continuum flux density at ∼230 GHz may be due to synchrotron radiation (**originating from obscured AGN and/or supernova remnants**) and free-free emission (Condon & Ransom (2016)). We can predict the contributions of these phenomena to our continuum flux by utilizing previous observations of our galaxies at lower frequencies where synchrotron and free-free emission dominate the flux, extrapolating their spectra to our frequencies. To estimate the contribution of synchrotron and free-free emission to our measured continuum flux, **we use 32.5 GHz integrated fluxes from Very Large array observations found in Barcos-Muñoz et al. (2017). Together with integrated ALMA Band 3 observations (project 2017.1.01235.S, PI Barcos-Muñoz), we can measure the**

spectral index of both synchrotron and free-free together between 32.5 and ∼100 GHz, then extrapolate the 100 GHz flux to ALMA Band 6 using that spectral index. For III Zw 035 the spectral index α = -0.58 ± 0.04 and for IRAS F01364−1042 α = -0.39 ± 0.04. Uncertainties are calculated as a combination of image noise and errors in calibration flux uncertainties for ALMA and the VLA (Diaz Trigo et al. 2019; Partridge et al. 2016).

To estimate the contribution of these contaminants to the Band 6 continuum, we use the ∼120 mas resolution, 32.5 GHz VLA data from Barcos-Muñoz et al. (2017) and the spectral indices mentioned prior. We extrapolate the 32.5 GHz integrated flux to a Band 6 flux density value using:

$$f_{\rm extra} = f_{\rm synch} + f_{\rm free-free} = f_{\rm 32.5GHz}\left(\frac{\nu_{\rm cont}}{\rm 32.5GHz}\right)^{\alpha} \quad (3)$$

where $\nu_{\rm cont}$ is the center of the continuum band for each galaxy in GHz, and the flux densities (f) are in Jy. The resulting contributions to our continuum flux by both synchrotron and free-free **sources** are **23%** and **34%** for III Zw 035 and IRAS F01364−1042 respectively.

These contributions are subtracted in the following equation, which adopts a modified blackbody spectral index $\beta = 1.8$, where we perform our gas mass conversion (Equation 3; Scoville et al. 2015):

$$\frac{0.868 \;\times\; ({\rm f_{cont}} - {\rm f_{extra}}){\rm d^2_{Mpc}}}{(1+z)^{4.8}{\rm T}_{25}\nu^{3.8}_{350}\Gamma_{RJ}10^3{\rm Mpc}}10^{10}{\rm M}_\odot \quad (4)$$

where the fluxes ($\rm f_{cont}$ is continuum flux density) are in mJy, luminosity distance, d, is in Mpc, T is normalized to 25 K, ν normalized to 350 GHz, and $\Gamma_{\rm RJ}$ is the correction for departure in the rest frame of the Planck function from Rayleigh-Jeans, which varies with temperature (Scoville et al. 2016).

Using two bracketing dust temperature cases, 100 K and 500 K, we find gas masses inside the 77 mas Keck-OSIRIS resolution (box) limit of $(1.00 \pm 4.29) \times 10^8$ $\rm M_\odot$ to $(5.24 \pm 0.22) \times 10^8$ $\rm M_\odot$ of mass for III Zw 035 and $(1.21 \pm 0.50) \times 10^8$ $\rm M_\odot$ to $(6.36 \pm 2.63) \times 10^8$ $\rm M_\odot$ of mass for IRAS F01364−1042 within 43.7 and 76.9 pc, respectively. **Rows 3 and 4 of Figure 3 show** the continuum flux density and molecular gas masses as a function of radius. Fractionally, in relation to the previously determined enclosed masses from Medling et al. (2015), these measured values account for as little as ∼ 5% in the high dust temperature case to as much as ∼75% in the low temperature case (see Table 2 for details). This wide range of gas masses and the topic of dust temperature are discussed within Section 6.2.

4.3. *Spectral index mapping*

To better understand the nature of the mm continuum emission in the nuclei of our galaxies, we create inter-band spectral index maps. To create such maps for our galaxies, we generate line-free continuum images for Band 3 (project 2017.1.01235.S, PI Barcos-Muñoz) and Band 6 (data presented here) with the same pixel and beam sizes and using a `robust` = −0.5. We then compute the spectral index per pixel defined as:

$$\alpha = \log\left(\frac{f_{\rm B6}}{f_{\rm B3}}\right)/\log\left(\frac{\nu_{\rm B6}}{\nu_{\rm B3}}\right) \quad (5)$$

where f is the flux density in Jy and ν is the frequency (GHz). B3 and B6 indicate the values of flux density and frequency of the images mentioned above. Data below rms of 3 is masked and not mapped. As a general rule, a positive mm spectral index favors dust emission (Planck Collaboration et al. 2016), while a steep negative mm spectral index indicates dominant synchrotron emission (see Section 4.2). We estimated the uncertainty of the spectral index via error propagation considering the uncertainty in the flux density due to noise in the image, plus 5

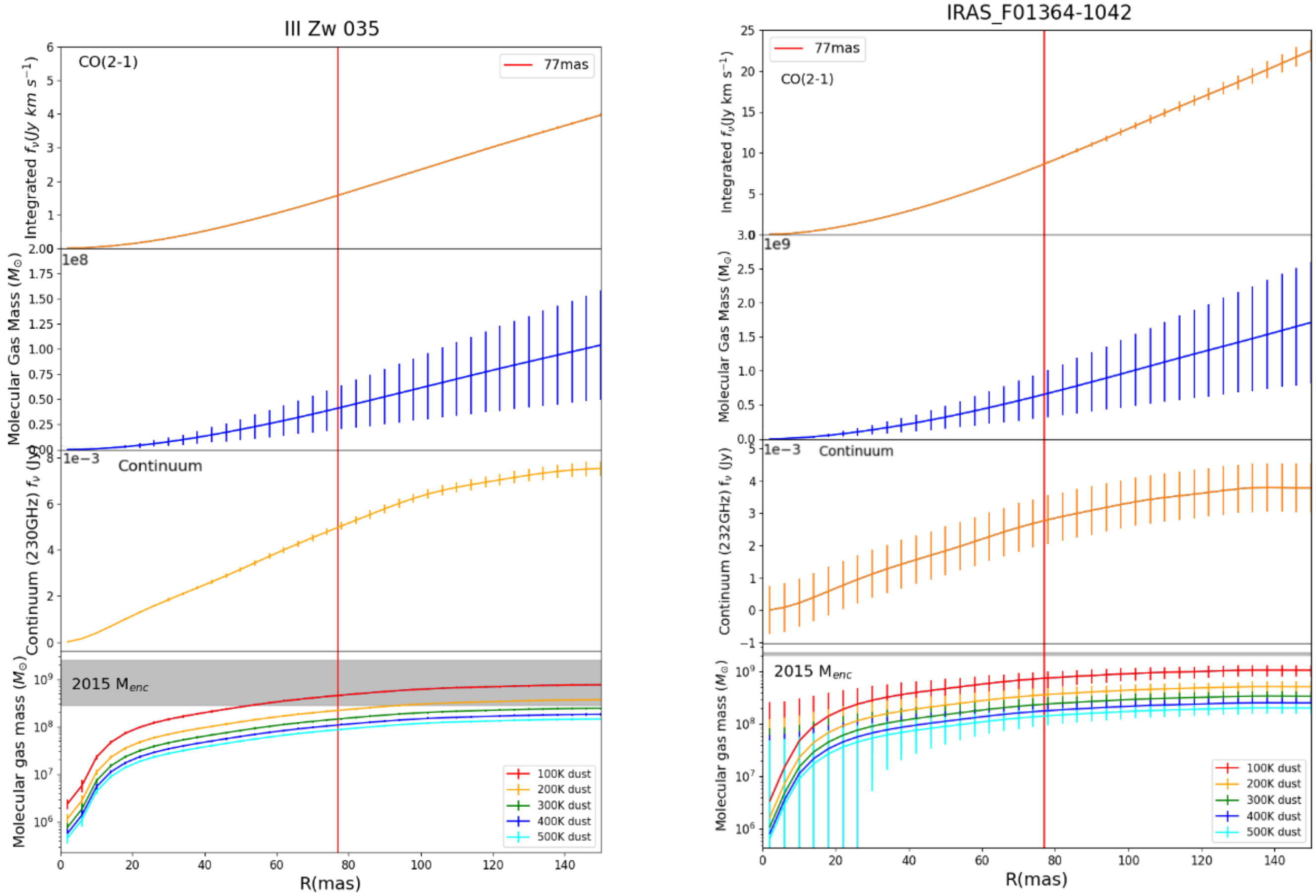

Figure 3. Integrated measurements and calculated masses within the boxed aperture for IRAS F01364−1042 and III Zw 035. *First row*: enclosed CO(2-1) flux from images described in Section 2. *Second row*: enclosed mass calculated from CO(2-1) fluxes shown in above panels using method described in Section 4.1. *Third row*: **integrated continuum flux densities at 230 GHz (III Zw 035) and 228 GHz (IRAS F01364−1042) extracted from images described in** Section 2. *Bottom row*: enclosed mass calculated from continuum fluxes shown in above panels using method described in Section 4.2. Grey regions are Medling et al. (2015) enclosed mass ranges. III Zw 035 requires a dust temperature above ∼175 K to have a dust-derived gas mass lower than the previous enclosed mass while IRAS F01364−1042 requires a dust temperature of >48 K.

and ∼10% errors due to the calibration flux uncertainties in ALMA Bands 3 and 6 respectively (Diaz Trigo et al. 2019).

In Figure 4, we show the spectral index maps and related error maps for both galaxies. Note that our estimates for synchrotron and free-free emission include the core along with emission from dust further away from it (see Section 6.2 for further discussion). Given the resolution restrictions of our spectral index maps, we don't have independent measurements of the spectral indices of the nuclei versus the clumpy torus-like structures in III Zw 035. **In both cases, the integrated spectral index values are positive in these nuclei. Alongside the f_{extra} measurements in Section 4.2 that estimate contribution fractions of free-free and synchrotron emission of <50%, these spectral index maps suggest that thermal dust emission is a major contributor to the Band 6 continuum emission over other non-thermal or free-free contribu-**

Integrated gas masses compared to previous enclosed mass measurements

		III Zw 035	IRAS F01364−1042
(1)M_{enc}	Gas (H_2, Brγ)	*	$(2.24^{+.06}_{-.17})\ \times 10^9$ $M_\odot$
	Stellar (disk)	$(>6.80^{+.10}_{-4.0})\ \times 10^8$ $M_\odot$	-
	Stellar (JAM)	$(<2.00^{+.50}_{-.70})\ \times 10^9$ $M_\odot$	-
(2)$M_{gas,CO}$		$(4.23 \pm 2.21) \times 10^7$ $M_\odot$	$(6.68 \pm 3.49) \times 10^8$ $M_\odot$
(4) Gas fraction		$<6.22\ ^{+1.7}_{-1.1}\%$ $>2.11\ ^{+1.2}_{-1.3}\%$	$29.8\ ^{+22.1}_{-22.2}\%$
(3)$M_{gas,cont(100K)}$		$(5.24 \pm 0.22) \times 10^8$ $M_\odot$	$(6.36 \pm 2.63) \times 10^8$ $M_\odot$
(4)Gas fraction		$>26.2\ ^{+9.2}_{-6.6}\%$ $<77.1\ ^{+45.4}_{-3.4}\%$	$28.3\ ^{+11.7}_{-11.9}\%$
(3)$M_{gas,cont(500K)}$		$(1.00 \pm 4.29) \times 10^8$ $M_\odot$	$(1.21 \pm 0.50) \times 10^8$ $M_\odot$
(4) Gas fraction		$>5.0\ ^{+1.3}_{-1.8}\%$ $<14.7\ ^{+8.7}_{-0.7}\%$	$5.4\ ^{+1.7}_{-1.2}\%$

Table 2. Summary of results for mass estimates via CO (α_{CO} method) and continuum. For III Zw 035 we compare to enclosed masses from stellar kinematics and in IRAS F01364−1042 we compare to enclosed masses from gas kinematics. *III Zw 035 gas-based dynamical masses exist in Medling et al. (2015), but we do not use them for comparison in this work due to likely contamination from a molecular outflow. (1): Enclosed masses from Medling et al. (2015). (2): Gas mass from CO(2-1) flux as calculated in Section 4.1. (3): Gas mass from continuum flux as calculated in Section 4.2. (4): Percentages displayed are relative to the kinematically-derived enclosed masses found in Medling et al. (2015) and are computed as M_{gas}/M_{enc}.

tions. Further observations at matched resolution to the Band 6 data are necessary to learn more about the radio SEDs of these cores and clumps to make a more direct comparison to our other results.

5. INDEPENDENT ENCLOSED MASS MEASUREMENTS

The results in Section 4 present corrected Medling et al. (2015) black hole masses for III Zw 035 and IRAS F01364−1042. With those corrections, the black holes remain overmassive except in the case of III Zw 035 with a sub∼175 K dust temperature. In this subsection, we independently measure enclosed masses at the Band 6 beam resolution using the CO cubes presented in this work.

5.1. *Tilted ring modeling*

To calculate dynamical, enclosed masses, **we model the CO kinematics using the** tilted-ring modeling algorithm ^{3D}Barolo (Di Teodoro & Fraternali 2015). Using our high resolution CO(2-1) cubes, ^{3D}Barolo models tilted rings with inclination-corrected rotational velocities to the line emission at a range of distances from the center. **Their 3D modeling approach is preferred over a 2D method in large part due to the instrumental effect of beam smearing being effectively removed during the convolution step (Di Teodoro & Fraternali 2015).** We provide initial guesses to ^{3D}Barolo's two-stage `3DFIT` task for parameters like inclination, PA, and redshift. We tested different methods of building the ^{3D}Barolo mask as well, using both SEARCH and SMOOTH&SEARCH. Models and residuals produced in this way are shown in

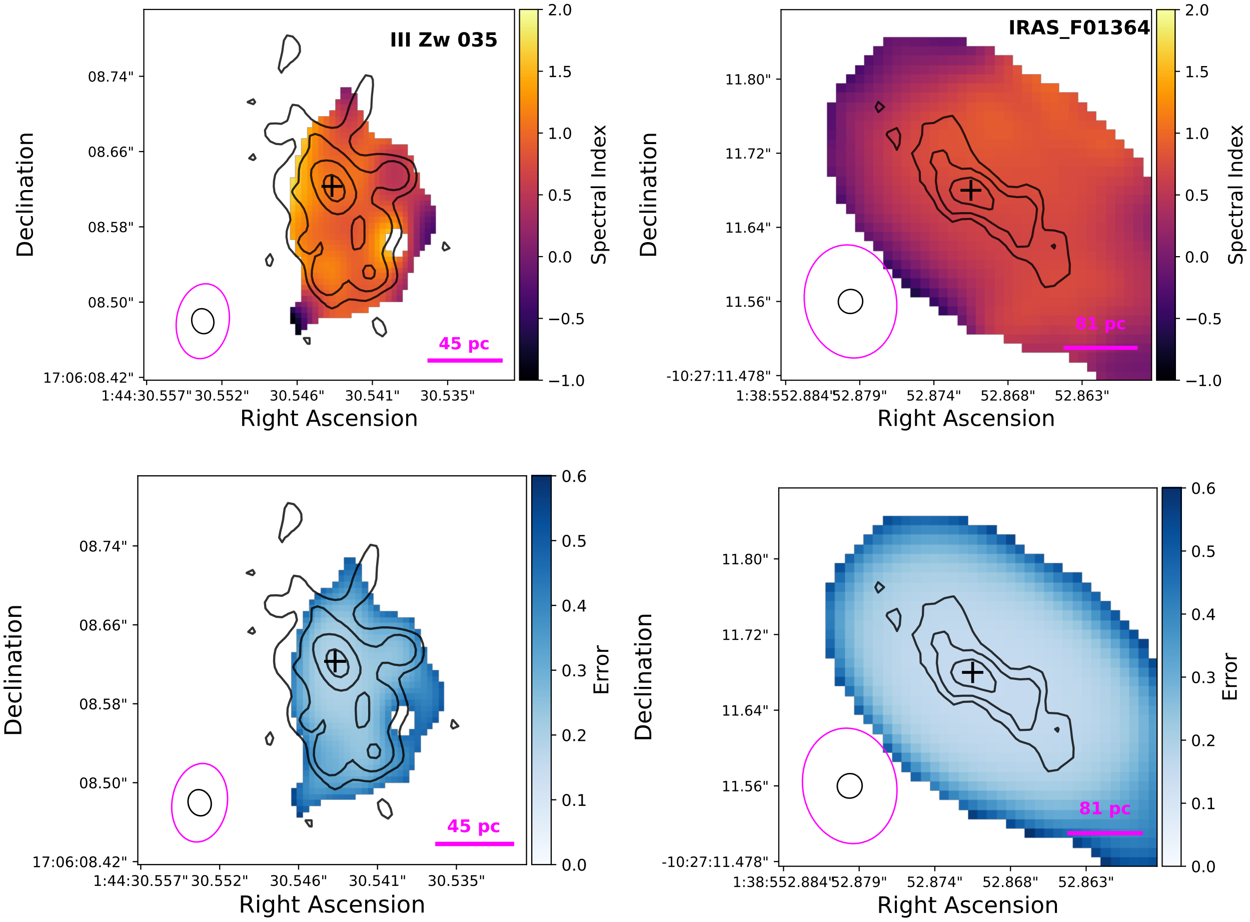

Figure 4. Spectral index (top) and uncertainty maps (bottom) for III Zw 035 (left) and IRAS F01364−1042 (right). The beam sizes of the continuum images used to create the spectral index maps (0.075" × 0.052" for III Zw 035 and 0.134" × 0.110" for IRAS F01364−1042) are shown in the lower left corners in magenta. The black contours correspond to the Band 6 combined line-free continuum emission at 230 GHz for III Zw 035 and 228 GHz for IRAS F01364−1042 with levels at 3, 6, 12, 24, 48 × (rms) Jy beam^{-1} (rms values are 32.9e-6 and 38.3e-6 for III Zw 035 and IRAS F01364−1042 respectively). Their beam sizes are shown in the lower left corners in black (31 x 25 mas for III Zw 035 and 29 x 28 mas for IRAS F01364−1042)

Appendix A. In III Zw 035, the outflow likely dominates the velocity dispersion map. Position angles modeled by ^{3D}Barolo are about 15 degrees lower than those in Medling et al. (2014). **This difference in PA may be due to the modeling in this work using kinematics of the cold gas rather than warm gas.**

We then use the inclination-corrected, circular velocities and radii of the kinematic models computed by ^{3D}Barolo in our enclosed mass calculation, $M_{enc} = R_{vmax} v^2 G^{-1}$, where M_{enc} is in kg, R is in m, v is m s^{-1} and **G is the gravitational constant**. This method assumes a spherical mass distribution. The enclosed mass profiles, along with the position-velocity models from ^{3D}Barolo and contours of position-velocity diagrams manually made in CARTA (Cube Analysis and Rendering Tool for Astronomy, Comrie et al. 2021), can be seen in Figure 5.

5.2. *Comparison to warm gas M_{enc}*

At 30 and 39 mas for III Zw 035 and IRAS F01364−1042 respectively, we find M_{enc} of $5.26^{+2.21}_{-2.10} \times 10^7$ and $2.09^{+.52}_{-.63} \times 10^8$ $M_\odot$(see Table 2) which are between 93-

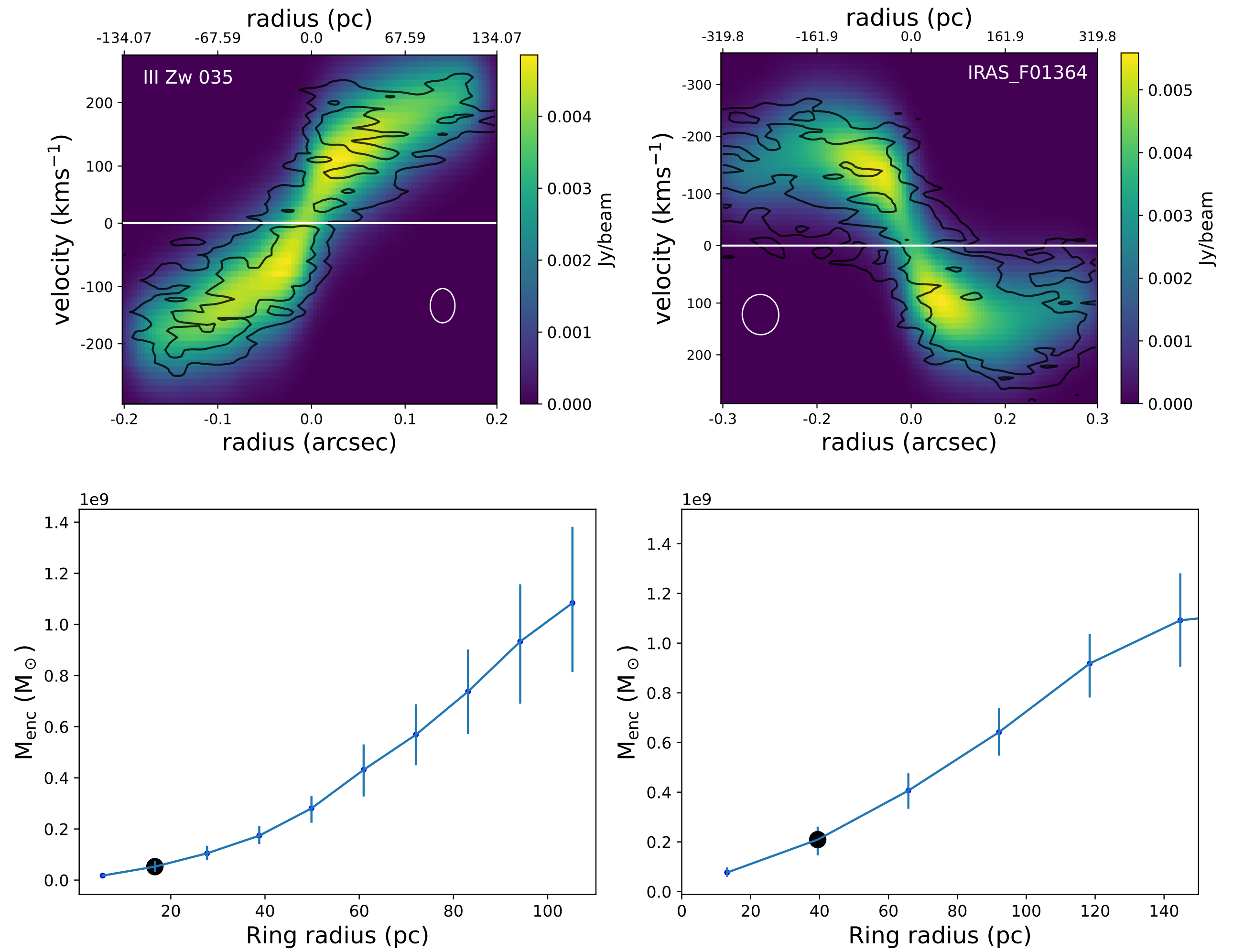

Figure 5. Position-velocity (PV) diagrams of the CO emission modeled across the major axis in III Zw 035 (left) & IRAS F01364−1042 (right). *Top:* PV models from [3D]Barolo outputs. Black contours correspond to 3, 6, 9, and 12 × rms of high resolution PV diagrams made in CARTA at the same central position with the same high resolution input cubes described in Section 2. **White ellipses represent the restoring beams of those data. The white, horizontal lines indicate the expected redshifted frequency of the CO(2-1) line with respect to the systemic velocities of the galaxies.** *Bottom:* Inclination-corrected enclosed masses calculated using the methods described in Section 5. **Enclosed masses were calculated on tilted-rings that were separated by their beam sizes. Both enclosed masses (at beam-sized radii indicated by the black circles) are about an order of magnitude lower than the measurements made in Medling et al. (2015).**

91% lower than those found in Medling et al. (2015) at 77 mas resolution. In Table 3, we show new estimates for the central M_{BH} by subtracting matched-resolution molecular gas masses from those high-resolution M_{enc}. Corrected M_{BH} are also compared to BH-galaxy scaling relations in Figure 6.

The first main difference that may be leading to different enclosed mass results between the modeling here and in Medling et al. (2015) is the nature of the kinematic tracer. In this work, we use CO(2-1), **which traces the cold gas in the nuclei of these galaxies while for IRAS F01364−1042 Medling et al. (2015) modeled the warm-gas tracer**

Integrated gas masses compared to enclosed masses measured in this work

	III Zw 035	IRAS F01364−1042
(1) $M_{enc,CO}$	$(5.26^{+2.21}_{-2.10}) \times 10^{7}\ M_{\odot}$	$(2.09^{+.52}_{-.63}) \times 10^{8}\ M_{\odot}$
(2) $M_{gas,CO}$	$(9.99 \pm 5.21) \times 10^{6}\ M_{\odot}$	$(2.38 \pm 1.24) \times 10^{8}\ M_{\odot}$
(4) Gas fraction	$19.0\ ^{+43.2}_{-41.1}\%$	$113.9\ ^{+64.3}_{-66.5}\%$
(3) $M_{gas,cont(100K)}$	$(2.00 \pm 0.98) \times 10^{8}\ M_{\odot}$	$(3.22 \pm 2.63) \times 10^{8}\ M_{\odot}$
(4) Gas fraction	$380.2\ ^{+191.0}_{-190.4}\%$	$154.1\ ^{+128.3}_{-129.4}\%$
(3) $M_{gas,cont(500K)}$	$(3.82 \pm 0.19) \times 10^{7}\ M_{\odot}$	$(6.13 \pm 5.02) \times 10^{7}\ M_{\odot}$
(4) Gas fraction	$69.8\ ^{+42.2}_{-40.0}\%$	$29.3\ ^{+34.6}_{-38.5}\%$

Table 3. Summary of results for mass estimates via CO (α_{CO} method) and continuum when subtracted from enclosed masses calculated in this work (see Section 5). All values in this table are measured at a radius equal to the beam size of the respective CO data. (1): Enclosed masses derived using CO(2-1) kinematics in Section 5. (2): Gas mass from CO(2-1) flux as calculated in Section 4.1. (3): Gas mass from continuum flux as calculated in Section 4.2. (4): Percentages displayed are relative to enclosed masses derived from CO kinematics and are calculated as $M_{gas}/M_{enc,CO}$.

Paα. Given the indication of outflows present in IRAS F01364−1042, Paα may be an unreliable tracer of the bulk motion of the gas (e.g. in Davies et al. 2024). In III Zw 035, although Medling et al. (2015) derived their masses from stars, which should not be impacted by outflows, the resolution of our cold gas dynamics is higher than obtained with Keck/OSIRIS. The CO beam sizes are 1.5-2 times smaller than the Keck/OSIRIS PSF. This means that we are physically probing **kinematics closer to** the black hole, thus presumably including less mass other than the black hole (stars, dust, gas) in the process.

The enclosed masses presented in this work have the **benefits of using a tracer of the dynamically cold gas and physically probing closer to the SMBH than the measurements of** Medling et al. (2015). Like the Medling et al. (2015) warm gas and stellar measurements **though**, for the purpose of comparison to scaling relations we remove the, these are **still measurements of** enclosed mass **(from which we can subtract gas mass)** rather than black hole mass.

6. DISCUSSION

6.1. *Black hole masses in context*

Figure 6 shows the black hole masses with our calculated nuclear gas contaminations removed on three scaling relations: M_{BH} vs. $\sigma_{\star}$, bulge luminosity L_{bulge}, and total stellar mass $M_{\star}$. For M_{BH} vs. $\sigma_{\star}$ we use dynamical data on elliptical and classical bulge galaxies compiled in Kormendy & Ho (2013) with **their equation** 7 for the best fit line. For M_{BH} vs. L_{bulge} we use luminosities from Marconi & Hunt (2003) and updated black hole masses from McConnell & Ma (2013) with an updated fit used in Medling et al. (2019). For M_{BH} vs. total stellar mass $M_{\star}$ we use data from Bennert et al. (2011) and Cisternas et al. (2011), along with a best fit line from McConnell & Ma (2013).

Results depend on the initial enclosed mass value used for these two nuclei. If we assume that the Medling et al. (2015) enclosed mass **(at coarser resolution)** is realistic, then the only case where we find enough molecular gas mass to shift either nucleus' dynamically-derived black hole mass down to scaling rela-

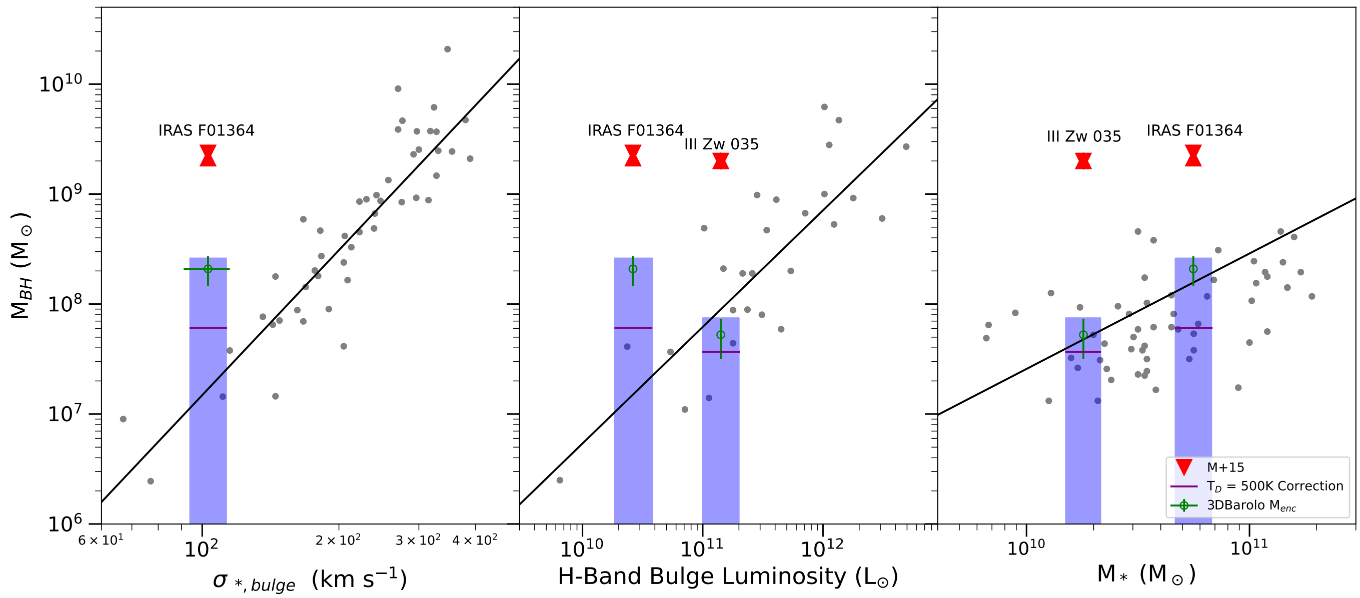

Figure 6. Medling et al. (2015) (red) and Section 5 (green) enclosed masses plotted on black hole scaling relations: $\mathrm{M_{BH}}$ vs. $\sigma_\star$ (left), bulge luminosity $\mathrm{L_{bulge}}$ (middle), and total stellar mass $\mathrm{M_\star}$ (right). Grey points and line fits are based on various literature measurements, see Section 6.1 for details. Blue shaded regions represent the widest range of molecular gas-corrected black hole masses ($\mathrm{M_{enc}}$ - $\mathrm{M_{gas}}$) where $\mathrm{M_{enc}}$ is the value computed in this work (see Section 5). Both the CO-derived gas value and the T_D = 100-500 K continuum methods are included in this range. The purple horizontal lines are the continuum corrected values with T_D = 500K. In all cases, the enclosed gas mass corrects the total enclosed mass measured in this work down to scaling relations.

tions is where III Zw 035's continuum-derived gas mass is below ∼175 K.

On the other hand, if we assume the dynamical modeling from Section 5 is better constrained, we find nearly the opposite. In all cases, subtracting the central molecular gas from the dynamical enclosed mass causes these black holes to fall on to scaling relations.

This dramatic distinction between the two methods could be caused by several factors. As is posited in Medling et al. (2015), non-circular motion could have an impact on those original BH mass measurements. Warm gas is more likely to trace the turbulent ouflow than cold gas**, which may have driven the $\mathbf{M_{enc}}$ from the warm gas up. Conversely, the $\mathbf{M_{enc}}$ derived in this work from the cold gas could lead to an underestimate due to dynamically cold gas disks being less susceptible to pressure support coming from turbulent motions (Barth et al. 2001; Walsh et al. 2013).** We find evidence for outflowing components along the minor axis in III Zw 035 and IRAS F01364−1042 in CO(2-1) at these small spatial scales. We also find evidence for **mild disk warping in both III Zw 035 and IRAS F01364−1042 in CO(2-1) moment maps, although primarily beyond the radius used to calculate $\mathbf{M_{enc}}$. The disk warping properties on the smallest scales remain unknown, and incorporating corrections for these kinematic deviations – especially for strong central inclination angle shifts** – could revise both of the enclosed mass measurements. Future work focused on these galaxies will provide additional information on the **magnitude of the non-circular motions caused by** the outflows, **which we can use to constrain their impact on these enclosed mass mea-**

surements (Song et al. in prep **for IRAS F01364−1042**).

6.2. *Uncertain Dust Temperature*

For our two galaxies, as with the gas, we do not have an accurate estimate for the dust temperature on the scales studied in this work. Our analysis uses the empirical calibration for dust temperature in ULIRGs from Scoville et al. (2016) in which gas mass scales inversely with temperature. Scoville et al. (2016) advocates for a mass-weighted T_D of 25 K based largely on Herschel observations of nearby galaxies (Dunne et al. 2011; Dale et al. 2012; Auld et al. 2013). Other studies in ULIRGs (e.g. Sakamoto et al. 2021 and Walter et al. 2022) have shown that submm luminosity-weighted dust temperatures can exceed 500 K in their nuclei. However, luminosity-weighted dust temperatures are always higher than their mass-weighted counterparts for which the Scoville et al. (2016) relation is calibrated.

This unknown presents a challenge for the results of our continuum-based measurements. As is shown in the bottom panel of Figure 3, depending on the temperature assumption, the **continuum-estimated** molecular gas mass has a ∼1.5 dex range for each galaxy. At low T_D, at both comparison radii, the **corresponding $\mathbf{M_{gas}}$** is driven *above even* the kinematic measurements from Medling et al. (2015). For III Zw 035 this temperature is ∼175 K and for IRAS F01364−1042 it is 48 K. If gas is the entirety of the enclosed mass in either case, it leaves no room for a SMBH or stellar component, so we consider these dust temperatures to be firm lower limits. As such, our continuum-based measurements are acting as an upper limit to the molecular gas mass content, and we must wait for more well-constrained dust temperature **estimates** for these galaxies **(perhaps using CO excitation diagrams or RADEX radiative transfer modelling at matched spatial scales, see ? for an example in NGC 1068)** to better understand the relationship between the two measurement methods.

6.3. *Implications for physics in nuclei of gas-rich mergers*

Whether or not these black holes still remain overmassive with respect to scaling relations depends on which enclosed mass is chosen. As we have discussed, there is reason to believe that because the cold gas measurements are theoretically less impacted by the turbulence caused by outflows, and because these data are at higher resolution, **the $\mathbf{M_{enc}}$ derived from CO gas-dynamical modeling are more reliable**. In this case, the new enclosed masses calculated in Section 5 **are upper limits on $\mathbf{M_{BH}}$, and both $\mathbf{M_{enc}}$ and $\mathbf{M_{enc}}$ - $\mathbf{M_{gas}}$ fall along** all scaling relations.

If we adopt values from Medling et al. (2015), those $\mathbf{M_{enc}}$ or $\mathbf{M_{enc}}$ - $\mathbf{M_{gas}}$ values all lie significantly above the scaling relations except for III Zw 035 when using a continuum-estimated $\mathbf{M_{gas}}$ with $\mathbf{T_D}$ $\lesssim$175 K. As was also found in Medling et al. (2019), kinematically-derived $\mathbf{M_{BH}}$ measurements upper limits in ULIRGs may be significantly elevated due to the unresolved (gaseous) mass surrounding SMBH. The impact of cold gas contamination will depend on the nature of each individual system. In the case of the two LIRGs studied here, **the fraction of the $\mathbf{M_{BH}}$ estimates from Medling et al. (2015) that can be attributed to cold gas** could be rather insignificant (2%) to very influential (75% or more depending on dust temperature and comparison value).

Evolutionarily for III Zw 035, IRAS F01364−1042, and NGC 6240N, **overmassive SMBHs** would suggest a model where black hole accretion occurs before growth on the larger galaxy scale. Simulations of this growth process suggest the opposite (Hopkins

2012; Cen 2012; Anglés-Alcázar et al. 2017). In merger-driven accretion, material has to travel to the nucleus, losing angular momentum along the way. On this path, there is expected to be a period of mixing and subsequent starburst that could cause global properties like $\sigma_\star$, L_{bulge}, and $M_\star$ to increase before the inflowing gas reaches the nucleus and accretes onto the SMBH. To explain a model where black hole mass can outpace stellar growth in a merger, an angular momentum dissipation mechanism to facilitate rapid accretion needs to be present.

The measurements presented here constrain M_{BH} corrections due to nuclear gas content to a lower limit. The current sample of four total nuclei (NGC6240 N/S, III Zw 035, and IRAS F01364−1042) is limited to these gas-rich mergers and is therefore still not representative or statistically large enough to make corrections to any general sample of SMBHs. In gas-rich LIRG mergers, at least a few to a few tens of percent of the **dynamically-measured M_{enc}** within a radius of 43-77 pc is gas that could be contaminating the M_{BH} measurements. This gas can be part of the circumnuclear disk, **dusty torus, or gaseous flows.** Galaxy models should incorporate black hole mass and the full distribution of nuclear gas to properly simulate accretion physics.

Large nuclear gas reservoirs (as are shown to form in gas-rich mergers) are likely to form a viscous accretion disk. which transports mass much slower than predicted by Bondi-like accretion **models theoretically predicated on free-fall of gas onto the SMBH** (Hoyle & Lyttleton 1939, Bondi & Hoyle 1944, Bondi 1952, Bisnovatyi-Kogan et al. 1979, Mayer et al. 2007, Power et al. 2011). We predict that models of gas-rich mergers that use a Bondi-like accretion prescription are overestimating accretion rates. Galactic nuclei can coalesce quicker than the larger scale disks, on timescales as short as 10 Myr (Khan et al. 2016). If their central SMBHs are to become overmassive, we hypothesize that SMBH accretion in systems like these should start early on in the merger timeline.

7. CONCLUSIONS

In this work we used high resolution (sub-30 mas) CO(2-1) and continuum observations of two nearby LIRGs, III Zw 035 and IRAS F01364−1042, to measure molecular gas mass within **the central few** 10s of pc. Fractionally, we find that between 1 and 75% of the enclosed masses calculated in Medling et al. (2015) from stellar or gas kinematics can be attributed to molecular gas within 10s of parsecs from the central black holes. **At higher resolution, the enclosed masses within the inner 40 mas are 91-93% lower than from kinematics taken over a larger region.** Molecular gas mass contributes at least 19% of the new enclosed mass.

Because of the higher resolution and less kinematically disturbed nature of cold gas, we expect the new dynamically-derived enclosed masses calculated in Section 5 to be closer to the true black hole mass of these merging systems. In all cases, starting from this enclosed mass, III Zw 035 and IRAS F01364−1042 fall on the black hole mass scaling relations shown in Figure 6. In most cases this is true even before subtracting the enclosed molecular gas mass. These new measurements are still limited in that they are enclosed masses rather than black hole masses, and our sample size is low. Very high resolution observations of cold gas for the remaining sample of overmassive black holes found in Medling et al. (2015) (IRAS F17207-0014, NGC 2623, and CGCG 436-030) and independent enclosed mass measurements of NGC 6240's nuclei would allow us to understand if these nuclei all fall on scaling relations when using cold gas as a tracer.

The accuracy of accretion modeling is directly limited by our understanding of typical nuclear gas masses and distributions. **With significant nuclear molecular gas, a viscous accretion disk is likely to form, causing a slower rate of accretion. However, the resulting non-spherical accretion could potentially also circumvent the Eddington limit; if super-Eddington accretion were common, it would have significant implications for the growth of supermassive black holes in the early universe and throughout cosmic time. Additionally, because many cosmological simulations rely on spherically-symmetric black hole accretion rate prescriptions, the presence of nuclear gas disks could limit their predictive power regarding the impacts of black hole growth and subsequent AGN feedback.** We need more high resolution datasets like the ones present here to push towards a unified picture of the average gas mass within galactic nuclei. Our current sample of four nuclei (NGC6240 N/S, III Zw 035, and IRAS F01364−1042) is not large enough nor representative of all gas-rich mergers. Regardless, gas should not be left unconsidered when using dynamics to derive black hole masses in gas-rich galaxies.

8. ACKNOWLEDGEMENTS

The authors thank first the indigenous people of Hawaiʻi for the opportunity to be guests on your sacred mountain. We recognize the cultural significance that Maunakea holds for your community and are privileged to use data borne from science conducted in such a setting. **We wish to pay respect to the Atacameño community of the Chajnantor Plateau, whose traditional home now also includes the ALMA observatory.**

We would like to thank the anonymous reviewer for their contributions to this project, in particular with regards to our **independent upper limit on black hole mass**. This work makes use of the following data from ALMA: projects 2018.1.01123.S and 2019.1.00811.S (PI: Medling); project 2017.1.01235.S (PI: Barcos-Muñoz). ALMA is a partnership of ESO (representing its member states), NSF (USA) and NINS (Japan), together with NRC (Canada) and NSC and ASIAA (Taiwan) and KASI (Republic of Korea), in cooperation with the Republic of Chile. The Joint ALMA Observatory is operated by ESO, AUI/NRAO and NAOJ. The National Radio Astronomy Observatory is a facility of the National Science Foundation operated under cooperative agreement by Associated Universities, Inc. Some of the data presented herein were obtained at the W. M. Keck Observatory, which is operated as a scientific partnership among the California Institute of Technology, the University of California and the National Aeronautics and Space Administration. The Observatory was made possible by the generous financial support of the W. M. Keck Foundation. The authors also wish to thank the W.M. Keck Observatory staff for their efforts on the OSIRIS+AO instrumentation. JA thanks the staff at NRAO Charlottesville for their generous mentorship during invaluable in-person visits and their assistance virtually. JA also thanks Enrico di Teodoro for his input on final model fits. JA acknowledges support from NRAO Student Observing Support program awards SOSPA7-017 and SOSPADA-017. JA and AMM also acknowledge support from NSF CAREER number 2239807. JA, AMM, and VU acknowledge partial funding support from the NASA Astrophysics Data Analysis Program (ADAP) grant number 80NSSC23K0750. VU further acknowledges partial funding support from NASA Astrophysics Data Analysis Program (ADAP) grant number 80NSSC20K0450, Space Telescope Science Institute grants, numbers HST-AR-17063.005-A, HST-GO- 17285.001, and JWST-GO-01717.001. Some of the data presented in this article was obtained from the

Mikulski Archive for Space Telescopes (MAST) at the Space Telescope Science Institute. The specific observations analyzed can be accessed via https://doi.org/10.17909/h5ts-qy16. JM is funded by the Hirsch Foundation. CR acknowledges support from the Fondecyt Iniciacion grant 11190831 and ANID BASAL project FB210003. The Flatiron Institute is supported by the Simons Foundation. CR acknowledges support from Fondecyt Regular grant 1230345 and ANID BASAL project FB210003.

Software: Astropy (Astropy Collaboration et al. 2013, 2018, 2022), Matplotlib (Hunter 2007), NumPy (Harris et al. 2020), CASA (CASA Team et al. 2022), and ^{3D}Barolo (Di Teodoro & Fraternali 2015).

REFERENCES

Anglés-Alcázar, D., Faucher-Giguère, C.-A., Quataert, E., Hopkins, P. F., Feldmann, R., Torrey, P., Wetzel, A., & Kereš, D. 2017, MNRAS, 472, L109

Armus, L., et al. 2009, PASP, 121, 559

Astropy Collaboration et al. 2013, A&A, 558, A33

—. 2018, AJ, 156, 123

—. 2022, ApJ, 935, 167

Auld, R., et al. 2013, MNRAS, 428, 1880

Barcos-Muñoz, L., et al. 2017, ApJ, 843, 117

Barth, A. J., Sarzi, M., Rix, H.-W., Ho, L. C., Filippenko, A. V., & Sargent, W. L. W. 2001, ApJ, 555, 685

Barth, A. J., Strigari, L. E., Bentz, M. C., Greene, J. E., & Ho, L. C. 2009, ApJ, 690, 1031

Beifiori, A., Courteau, S., Corsini, E. M., & Zhu, Y. 2012, MNRAS, 419, 2497

Bennert, V. N., Auger, M. W., Treu, T., Woo, J.-H., & Malkan, M. A. 2011, ApJ, 742, 107

Bennert, V. N., et al. 2021, ApJ, 921, 36

Bentz, M. C., et al. 2013, ApJ, 767, 149

Bisnovatyi-Kogan, G. S., Kazhdan, Y. M., Klypin, A. A., Lutskii, A. E., & Shakura, N. I. 1979, Soviet Ast., 23, 201

Bolatto, A. D., Wolfire, M., & Leroy, A. K. 2013, ARA&A, 51, 207

Bondi, H. 1952, MNRAS, 112, 195

Bondi, H., & Hoyle, F. 1944, MNRAS, 104, 273

Briggs, D. S. 1995, in American Astronomical Society Meeting Abstracts, Vol. 187, American Astronomical Society Meeting Abstracts, 112.02

Burton, W. B., Gordon, M. A., Bania, T. M., & Lockman, F. J. 1975, ApJ, 202, 30

Cackett, E. M., Bentz, M. C., & Kara, E. 2021, iScience, 24, 102557

Cappellari, M. 2008, MNRAS, 390, 71

CASA Team et al. 2022, PASP, 134, 114501

Cen, R. 2012, ApJ, 755, 28

Cicone, C., et al. 2018, ApJ, 863, 143

Cisternas, M., et al. 2011, ApJL, 741, L11

Clavel, J., et al. 1991, ApJ, 366, 64

Combes, F. 1991, ARA&A, 29, 195

Comrie, A., et al. 2021, CARTA: The Cube Analysis and Rendering Tool for Astronomy

Condon, J. J., & Ransom, S. M. 2016, Essential Radio Astronomy

Cortes, P. A., et al. 2023, ALMA Cycle 10 Technical Handbook (Cycle 10; Doc. 10.3; version 1.1), Zenodo. https://doi.org/10.5281/zenodo.7822943

Cretton, N., de Zeeuw, P. T., van der Marel, R. P., & Rix, H.-W. 1999, ApJS, 124, 383

Dale, D. A., et al. 2012, ApJ, 745, 95

Davies, R., et al. 2024, A&A, 689, A263

Davis, B. L., Graham, A. W., & Cameron, E. 2018, ApJ, 869, 113

—. 2019, ApJ, 873, 85

Di Teodoro, E. M., & Fraternali, F. 2015, MNRAS, 451, 3021

Diaz Trigo, M., Carpenter, J., Maude, L., Miura, R., & Plunkett, A. 2019, ALMA Cycle 7 Proposer's Guide, 2019, ALMA Cycle 7 Proposer's Guide, ALMA Doc. 7.2 v1.0 : Proposer's guide for the Atacama Large Millimeter/Submillimeter Array (ALMA) Cycle 7, Doc. 7.2, ver. 1.0, 2019

Dickman, R. L. 1978, ApJS, 37, 407

Dunne, L., et al. 2011, MNRAS, 417, 1510

Event Horizon Telescope Collaboration et al. 2019, ApJL, 875, L1

Faber, S. M., & Jackson, R. E. 1976, ApJ, 204, 668

García-Burillo, S., et al. 2021, A&A, 652, A98

Gebhardt, K., et al. 2000, ApJL, 539, L13

Genzel, R., Eisenhauer, F., & Gillessen, S. 2010, Reviews of Modern Physics, 82, 3121

Ghez, A. M., et al. 2008, ApJ, 689, 1044

Gültekin, K., et al. 2009, ApJ, 698, 198

Häring, N., & Rix, H.-W. 2004, ApJL, 604, L89

Harris, C. R., et al. 2020, Nature, 585, 357

Heckman, T. M., & Best, P. N. 2014, ARA&A, 52, 589

Herrero-Illana, R., et al. 2019, A&A, 628, A71

Hinshaw, G., et al. 2009, ApJS, 180, 225

Ho, L. 1999, in Astrophysics and Space Science Library, Vol. 234, Observational Evidence for the Black Holes in the Universe, ed. S. K. Chakrabarti, 157

Hopkins, P. F. 2012, MNRAS, 420, L8

Hopkins, P. F., Cox, T. J., Kereš, D., & Hernquist, L. 2008a, ApJS, 175, 390

Hopkins, P. F., Hernquist, L., Cox, T. J., & Kereš, D. 2008b, ApJS, 175, 356

Horne, K., Peterson, B. M., Collier, S. J., & Netzer, H. 2004, PASP, 116, 465

Hoyle, F., & Lyttleton, R. A. 1939, Proceedings of the Cambridge Philosophical Society, 35, 405

Hunter, J. D. 2007, Computing in Science & Engineering, 9, 90

Khan, F. M., Fiacconi, D., Mayer, L., Berczik, P., & Just, A. 2016, ApJ, 828, 73

Kormendy, J. 1993, in The Nearest Active Galaxies, ed. J. Beckman, L. Colina, & H. Netzer, 197–218

Kormendy, J., & Gebhardt, K. 2001, in American Institute of Physics Conference Series, Vol. 586, 20th Texas Symposium on relativistic astrophysics, ed. J. C. Wheeler & H. Martel, 363–381

Kormendy, J., & Ho, L. C. 2013, ARA&A, 51, 511

Kormendy, J., et al. 1997, ApJL, 482, L139

Lauer, T. R., et al. 1995, AJ, 110, 2622

Lutz, D., et al. 2020, A&A, 633, A134

Magorrian, J., et al. 1998, AJ, 115, 2285

Marconi, A., & Hunt, L. K. 2003, ApJL, 589, L21

Mayer, L., Kazantzidis, S., Madau, P., Colpi, M., Quinn, T., & Wadsley, J. 2007, Science, 316, 1874

McConnell, N. J., & Ma, C.-P. 2013, ApJ, 764, 184

McLure, R. J., & Dunlop, J. S. 2002, MNRAS, 331, 795

Medling, A. M., Ammons, S. M., Max, C. E., Davies, R. I., Engel, H., & Canalizo, G. 2011, ApJ, 743, 32

Medling, A. M., et al. 2014, ApJ, 784, 70

—. 2015, ApJ, 803, 61

—. 2019, ApJL, 885, L21

Merritt, D., & Ferrarese, L. 2001, MNRAS, 320, L30

Mirabel, I. F., & Sanders, D. B. 1988, ApJ, 335, 104

Montoya Arroyave, I., et al. 2023, A&A, 673, A13

Morgan, C. W., Kochanek, C. S., Morgan, N. D., & Falco, E. E. 2010, ApJ, 712, 1129

Partridge, B., López-Caniego, M., Perley, R. A., Stevens, J., Butler, B. J., Rocha, G., Walter, B., & Zacchei, A. 2016, ApJ, 821, 61

Pihlström, Y. M., Conway, J. E., Booth, R. S., Diamond, P. J., & Polatidis, A. G. 2001, A&A, 377, 413

Planck Collaboration et al. 2016, A&A, 596, A104

Power, C., Nayakshin, S., & King, A. 2011, MNRAS, 412, 269

Sakamoto, K., Martín, S., Wilner, D. J., Aalto, S., Evans, A. S., & Harada, N. 2021, ApJ, 923, 240

Sanders, D. B., & Mirabel, I. F. 1996, ARA&A, 34, 749

Sandstrom, K. M., et al. 2013, ApJ, 777, 5

Schwarzschild, M. 1979, ApJ, 232, 236

Scoville, N., et al. 2015, ApJ, 800, 70

—. 2016, ApJ, 820, 83

Scoville, N. Z., & Solomon, P. M. 1975, ApJL, 199, L105

Silk, J., & Rees, M. J. 1998, A&A, 331, L1

Solomon, P. M., Scoville, N. Z., Penzias, A. A., Wilson, R. W., & Jefferts, K. B. 1972, ApJ, 178, 125

Solomon, P. M., & Vanden Bout, P. A. 2005, ARA&A, 43, 677

Stierwalt, S., et al. 2013, ApJS, 206, 1

Teng, Y.-H., et al. 2022, ApJ, 925, 72

Tremaine, S., et al. 2002, ApJ, 574, 740

U, V., et al. 2012, ApJS, 203, 9

—. 2013, ApJ, 775, 115

—. 2019, ApJ, 871, 166

—. 2022, ApJ, 925, 52

van den Bosch, R. C. E., van de Ven, G., Verolme, E. K., Cappellari, M., & de Zeeuw, P. T. 2008, MNRAS, 385, 647

Vestergaard, M., & Peterson, B. M. 2006a, ApJ, 641, 689

—. 2006b, ApJ, 641, 689

Walsh, J. L., Barth, A. J., Ho, L. C., & Sarzi, M. 2013, ApJ, 770, 86

Walsh, J. L., van den Bosch, R. C. E., Barth, A. J., & Sarzi, M. 2012, ApJ, 753, 79

Walter, F., et al. 2022, ApJ, 927, 21

Wang, J., Zhang, Z., & Shi, Y. 2011, MNRAS, 416, L21

Wilson, W. J., Schwartz, P. R., Epstein, E. E., Johnson, W. A., Etcheverry, R. D., Mori, T. T., Berry, G. G., & Dyson, H. B. 1974, ApJ, 191, 357

Wright, E. L. 2006, PASP, 118, 1711

Yoon, I. 2017, MNRAS, 466, 1987

APPENDIX

A. KINEMATIC MODELING

This section of the Appendix describes additional detail about the ^{3D}Barolo tilted ring modeling used in this work to calculate enclosed masses from the cold CO gas. ^{3D}Barolo is a tilted-ring modeling algorithm with a task called `3DFIT`. This algorithm takes in data with kinematic information, and derives rotational velocities for tilted rings spaced at intervals specified by the user. For our purposes with the high resolution CO(2-1) cubes, we use `3DFIT` in two-stage mode. In two-stage mode `3DFIT` regularizes the input parameters, then enters a second fitting phase (Di Teodoro & Fraternali 2015).

We tested different methods of building the `3DFIT` mask (used by the program to determine where there is genuine emission), using both SEARCH and SMOOTH&SEARCH, and we tested different input parameters (e.g. PA, inclination, redshift, and systemic velocity). In testing, as is suggested by the authors of ^{3D}Barolo, we judge model goodness by examining the line intensity maps and PV plots (as in Figure 5). Models and residuals produced in this way are shown in Appendix A, and output tilted ring parameters can be found in Table 4. We use the resulting rotational velocities in Section 5 to calculate enclosed masses.

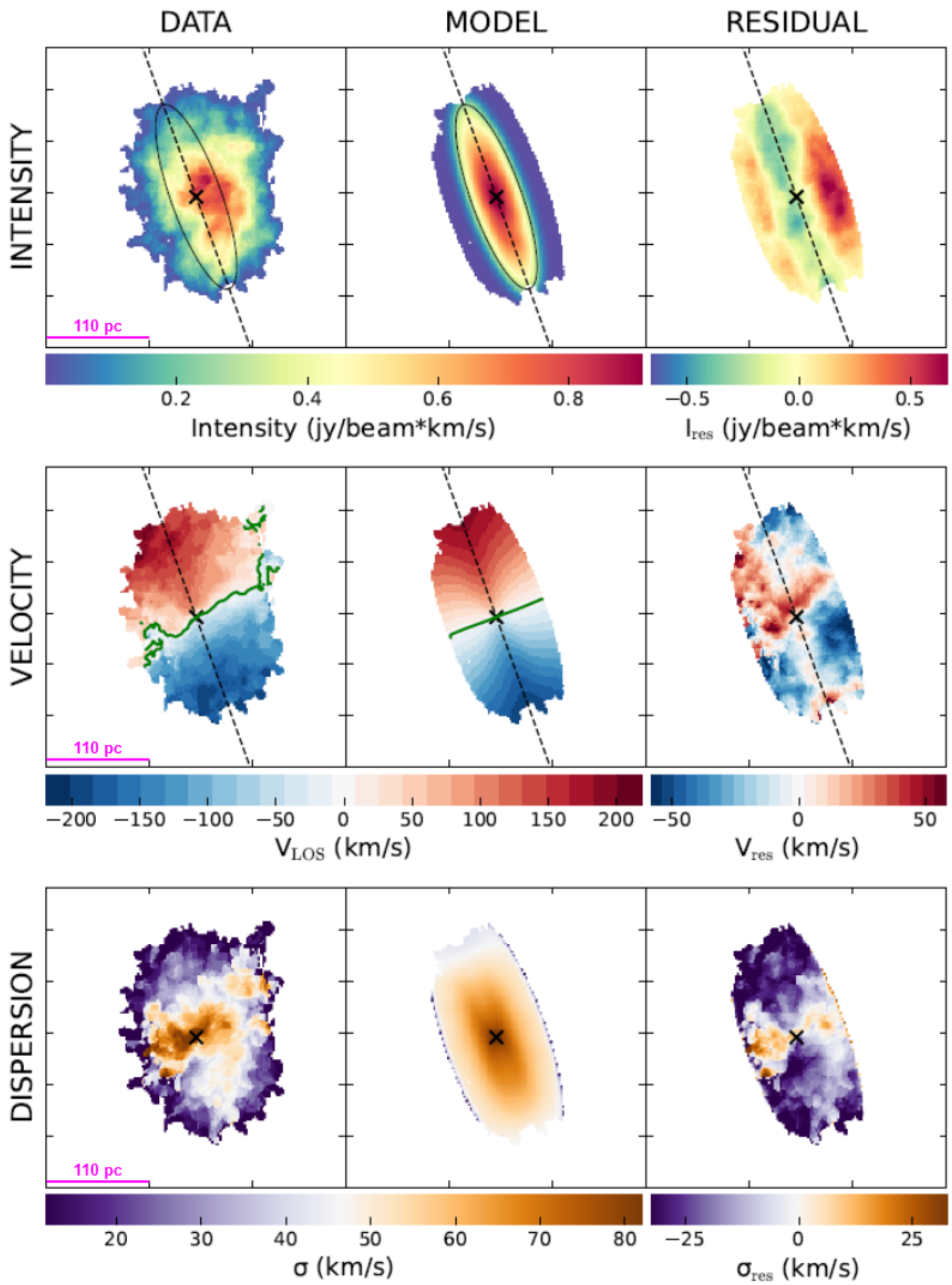

Figure 7. III Zw 035 ring models produced by ^{3D}Barolo, used to calculate enclosed masses in Section 5. Input CO(2-1) images are the same as presented in Figure 2 (33 x 28 mas beam size), and input parameters include PA, inclination, redshift, and systemic velocity. Ring model output parameters can be found in Table 4. Green lines in the first two velocity panels indicate 0 km s^{-1}, which indicate potential disk-warping. III Zw 035's velocity dispersion component is likely dominated by the outflow.

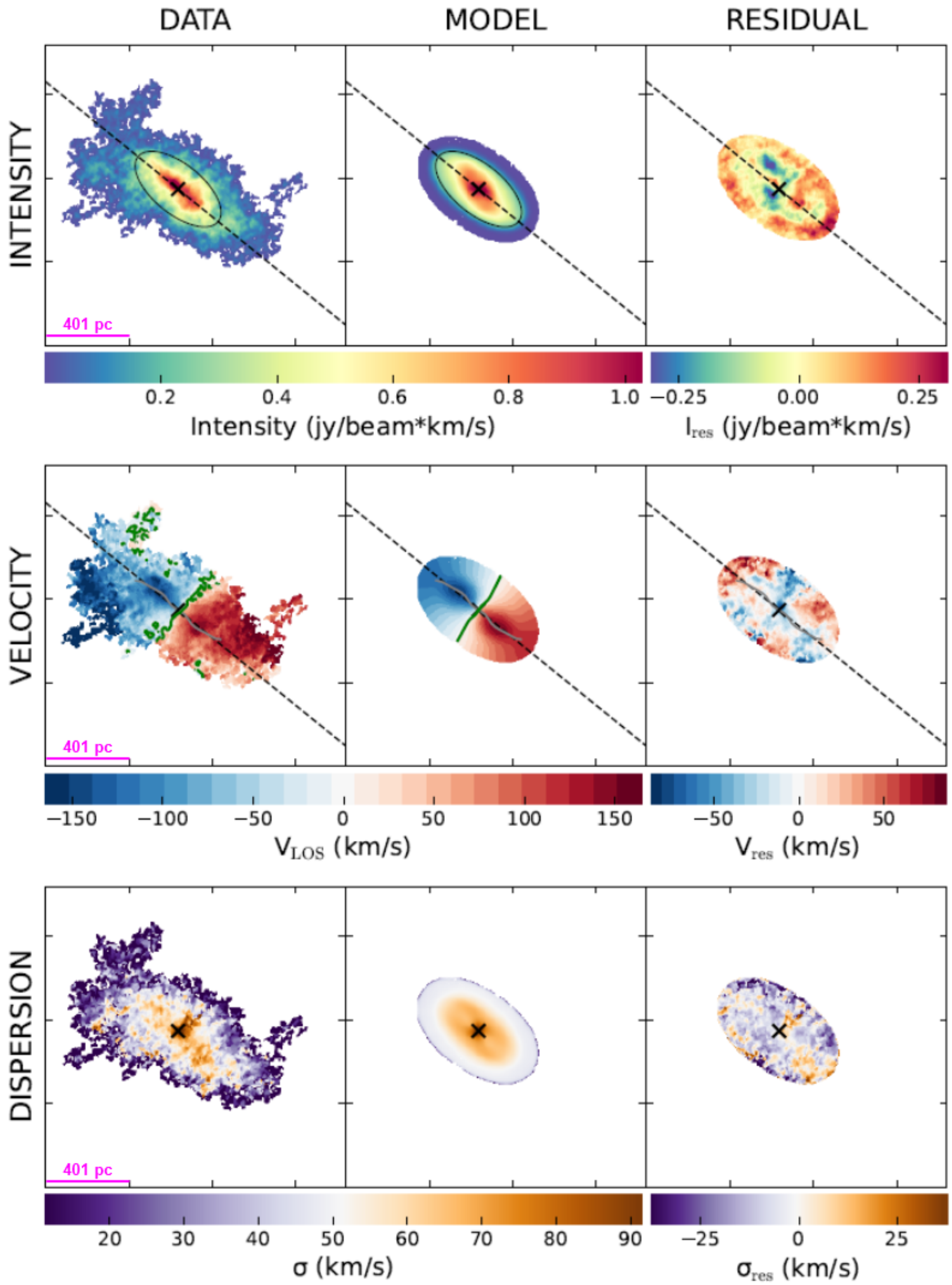

Figure 8. IRAS F01364−1042 ring models produced by ^{3D}Barolo, used to calculate enclosed masses in Section 5. Input CO(2-1) images are the same as presented in Figure 2 (42 x 39 mas beam size), and input parameters include PA, inclination, redshift, and systemic velocity. Ring model output parameters can be found in Table 4. Green lines in the first two velocity panels indicate 0 km s^{-1}. IRAS F01364−1042 is particularly well-defined by a rotating disk, although residuals show some evidence of outflows along the minor axis in velocity space.

Galaxy	R (arcsec)	v_{rot} (km s^{-1})	σ_v (km s^{-1})
III Zw 035	0.010	$117.299^{+15.688}_{-16.559}$	$12.962^{+13.157}_{-13.157}$
	0.030	$116.632^{+24.541}_{-23.268}$	$70.446^{+13.758}_{-13.758}$
	0.050	$127.537^{+17.974}_{-15.995}$	$71.341^{+13.321}_{-11.454}$
	0.070	$138.887^{+14.576}_{-13.268}$	$64.466^{+11.887}_{-9.568}$
	0.090	$155.569^{+13.731}_{-15.584}$	$66.102^{+11.342}_{-12.737}$
	0.110	$174.523^{+20.043}_{-21.25}$	$67.762^{+14.458}_{-14.458}$
	0.130	$184.272^{+19.313}_{-19.348}$	$58.828^{+12.395}_{-12.395}$
	0.150	$195.405^{+21.794}_{-22.034}$	$60.046^{+12.700}_{-12.700}$
	0.170	$206.447^{+24.747}_{-26.912}$	$56.457^{+12.373}_{-13.456}$
	0.190	$210.448^{+28.939}_{-26.236}$	$44.030^{+14.469}_{-13.118}$
IRAS F01364−1042	0.013	$158.335^{+21.370}_{-17.959}$	$30.945^{+11.350}_{-11.103}$
	0.039	$150.972^{+18.810}_{-22.804}$	$65.695^{+14.215}_{-14.215}$
	0.065	$162.998^{+13.971}_{-14.571}$	$61.799^{+9.680}_{-9.638}$
	0.091	$173.123^{+13.000}_{-12.731}$	$62.743^{+8.393}_{-8.159}$
	0.117	$182.589^{+11.929}_{-13.586}$	$63.689^{+8.303}_{-9.952}$
	0.143	$180.143^{+15.618}_{-15.427}$	$64.256^{+10.198}_{-10.775}$
	0.169	$168.557^{+18.185}_{-18.222}$	$61.354^{+10.996}_{-11.841}$
	0.195	$152.269^{+22.261}_{-20.124}$	$57.424^{+12.634}_{-13.882}$
	0.221	$133.305^{+23.109}_{-22.004}$	$53.216^{+11.214}_{-11.214}$
	0.247	$137.034^{+23.665}_{-26.155}$	$45.981^{+12.003}_{-12.003}$

Table 4. ^{3D}Barolo phase two best fit tilted ring model parameters for III Zw 035 and IRAS F01364−1042. The velocity dispersion modeling (column 4) should be taken with caution because of the likely dominance of it by the outflows in these galactic nuclei. The second and third columns, tilted ring radius and rotational velocity, are used to compute enclosed masses as found in Section 5.